Nanoscale Advances

ROYAL SOCIETY OF CHEMISTRY

PAPER

View Article Online
View Journal | View Issue

Cite this: *Nanoscale Adv.*, 2025, **7**, 6864

Hexagonal ABX_3 nanocrystals: rod-shaped $BaNbS_3$ and $BaTaS_3$; $BaTiSe_3$, $BaZrSe_3$, and other selenide derivatives for optoelectronic applications

Shubhanshu Agarwal, [a] Sofia Rodriguez Perilla, [b] Matheus Rios Marques,[c] Daniel C. Hayes, [a] Kiruba Catherine Vincent [a] and Rakesh Agrawal *[a]

Received 27th June 2025
Accepted 9th September 2025

DOI: 10.1039/d5na00628g

rsc.li/nanoscale-advances

Chalcogenide perovskites have increasingly garnered attention in recent years for various optoelectronic applications. While distorted perovskites such as $BaZrS_3$ are primarily being explored for photovoltaic applications, hexagonal ABS_3 compounds such as $BaTiS_3$ have been proposed for optical devices and thermoelectrics due to their intriguing properties arising from their quasi-1D structure, which imparts anisotropy in properties. However, other members of the hexagonal family remain largely unexplored, likely due to their harsh synthesis conditions. In this report, we synthesize nanocrystals of relatively unexplored members of the hexagonal ABX_3 chalcogenides family, which also possess a similar rod-like morphology and could be useful for polarized photodetection applications. Specifically, we modified our previously reported sulfide perovskite nanoparticle synthesis route to produce $BaNbS_3$ and $BaTaS_3$ nanocrystals. Furthermore, we explored selenium and selenourea as precursors to synthesize selenide hexagonal nanocrystals such as $BaTiSe_3$ and $BaZrSe_3$, as well as other selenide analogues like $Ba_3Nb_2Se_9$ and $Ba_3Ta_2Se_9$. This marks the first report of nanocrystal synthesis for the $BaMSe_3$ family, where M is an early transition metal.

Introduction

In an ever-evolving technological world, semiconductors are being actively used for various applications, ranging from photodetectors and sensors to photonic and optoelectronic devices, among others.[1,2] Consequently, there is a pressing need to discover and utilize novel semiconductors for these applications. Recently, the chalcogenide perovskite family has garnered increasing attention due to its remarkable optical properties.[3,4] While distorted perovskite members such as $BaZrS_3$ are being extensively explored for photovoltaic applications owing to their suitable bandgap, high light absorption, and stability, the hexagonal members of this family, such as $BaTiS_3$, represent a quasi-one-dimensional (quasi-1D) ternary chalcogenide. This structure is characterized by chains of face-sharing TiS_6 octahedra along the *c*-axis, with Ba^{2+} cations interspersed between these chains. A comparison of the structure of $BaZrS_3$ and $BaTiS_3$ is shown in Fig. 1.

This structural arrangement imparts strong optical and electronic anisotropy, resulting in unique properties such as giant birefringence (up to 0.76 in the mid-infrared) and dichroism spanning from the visible to mid-infrared spectral ranges.[5–8] The pronounced anisotropy and broad spectral response of $BaTiS_3$ make it highly suitable for polarization-sensitive photodetectors, particularly in the near-infrared (NIR) range. Additionally, the anisotropy facilitates highly directional charge transport, with reported electron mobilities exceeding 300 $cm^2 V^{-1} s^{-1}$ along the *c*-axis, further enhancing its potential for polarization-sensitive photodetectors, photonic devices, and optoelectronic applications. $BaTiS_3$ also exhibits anisotropy in thermal transport properties and demonstrates exceptionally low, glass-like thermal conductivity, attributed to the dynamic behavior of Ti^{4+} cations within a shallow double potential well.[9–12] This combination of low thermal conductivity and reasonable electronic mobility is advantageous for thermoelectric applications, where a high figure of merit (*ZT*) is critical. Furthermore, $BaTiS_3$ has been predicted to have high absorbance ($\sim 10^5$ cm^{-1}), underscoring its potential as an efficient light absorber.[13]

The structural anisotropy in $BaTiS_3$ is rooted in the chains of face-sharing TiS_6 octahedra along the *c*-axis, favoring the formation of needle- or rod-shaped crystals and imparting unique optoelectronic properties.[7,15–17] Similar to $BaTiS_3$, $Sr_{1.143}TiS_3$ has also shown high anisotropy and birefringence and is being actively explored for various other applications.[18,19] While these two materials have garnered attention, other members of the hexagonal ABS_3 family-such as $BaTaS_3$, $BaNbS_3$, and their selenide derivatives, which also crystallize in a rod-

[a]*Davidson School of Chemical Engineering, Purdue University, West Lafayette, IN 47907, USA. E-mail: agrawalr@purdue.edu*

[b]*Chemical and Environmental Engineering, Universidad Nacional de Colombia, Bogota D.C., Colombia*

[c]*Chemical Engineering Program, Federal University of Rio de Janeiro, Rio de Janeiro, 21941-853, Brazil*

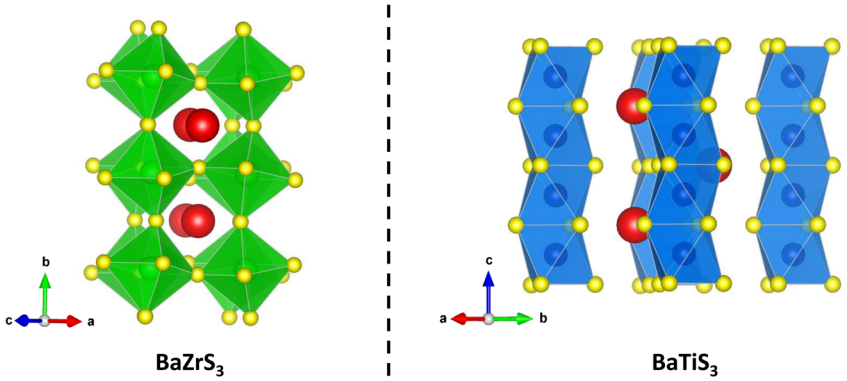

Fig. 1 The structures of $BaZrS_3$ and $BaTiS_3$ are shown. Ba atoms are illustrated in red, Zr atoms in green, Ti atoms in blue, and S atoms in yellow. $BaZrS_3$ crystallizes in an orthorhombic lattice with the *Pnma* space group, whereas $BaTiS_3$ is shown in a hexagonal lattice with the $P6_3/mmc$ space group. The structures are drawn using VESTA.[14]

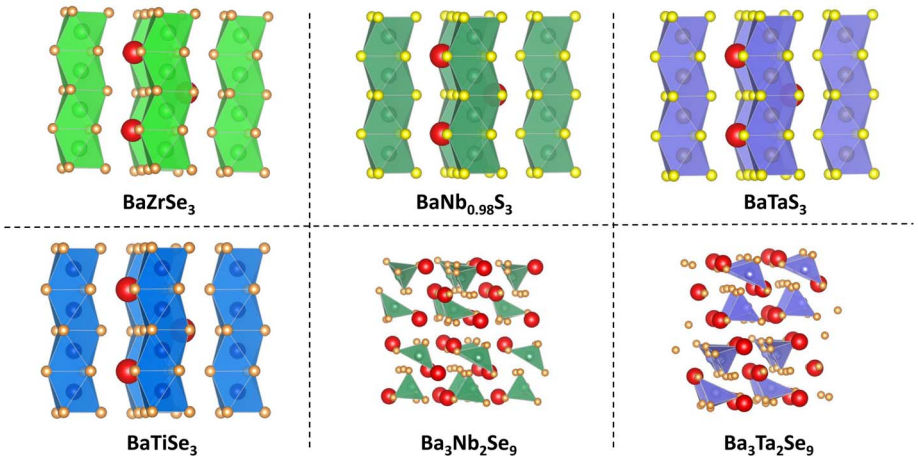

Fig. 2 The structures of $BaZrSe_3$, $BaNb_{0.98}S_3$, $BaTaS_3$, $BaTiSe_3$, $Ba_3Nb_2Se_9$ and $Ba_3Ta_2Se_9$ are shown. Ba atoms are illustrated in red, Zr atoms in light green, Nb atoms in olive green, Ta atoms in purple, Ti atoms in blue, S atoms in yellow and Se atoms in orange. $BaZrSe_3$, $BaNb_{0.98}S_3$, $BaTaS_3$ and $BaTiSe_3$ crystallizes in a hexagonal lattice with the $P6_3/mmc$ space group. On the other hand, $Ba_3Nb_2Se_9$ and $Ba_3Ta_2Se_9$ crystallizes in a monoclinic lattice with $P12_1/c1$ space group. The structures are drawn using VESTA.[14]

like morphology with quasi-1D structure and hexagonal lattice could potentially show similarly exhilarating performance. $BaTiSe_3$ has also been reported to exhibit giant birefringence, but it has been studied only sparingly.[20] However, in the chalcogenide perovskite literature, the synthesis of this class of materials has been challenging and often relies on high-temperature synthesis, serving as a barrier to the study of many potentially attractive materials.[3,16]

In this regard, we have attempted the synthesis of nanocrystals of Ba–Nb–S, Ba–Nb–Se, Ba–Ta–S, Ba–Ta–Se, Ba–Ti–Se and Ba–Zr–Se members of this family at temperatures below 380 °C. This marks the first report on nanocrystal synthesis of selenide members of the $BaMSe_3$ compounds. The crystal structures of each nanocrystal synthesized in this report are shown in Fig. 2. The report also sheds light on the bandgaps of $BaNbS_3$ and $BaTaS_3$, which have not previously been conclusively reported in the literature. While Sr–Ti–Se synthesis was also attempted, it resulted in binary compounds with the methods utilized in this work. It should be noted that all successful nanocrystal syntheses in this work have been reported with their nominal compositions; however, it is likely that some or all of them have off-stoichiometric compositions, as commonly observed for hexagonal ABX_3 compounds.[21–24]

Results and discussion

As previously mentioned, hexagonal ABX_3 compounds are increasingly finding utility in many applications, yet many members of this family remain largely unexplored, likely due to known difficulties in synthesizing ternary chalcogenides with early transition metal members. Here, we demonstrate nanocrystal synthesis of these materials with their characteristic rod-like morphology at temperatures below 380 °C. While $BaTiS_3$ nanocrystals have been synthesized previously,[15,17,25] other hexagonal variants such as $BaNbS_3$, $BaTaS_3$, and their respective selenides have only been synthesized *via* solid state reactions.[23,26–33]

Synthesis of $BaMS_3$ nanocrystals (M = Nb, Ta)

For this work, organometallic precursors of Ba, Nb, and Ta-specifically bis(pentamethylcyclopentadienyl)barium (Cp^*_2Ba), pentakis(dimethylamido)niobium (PDMAN), and pentakis(dimethylamido)tantalum (PDMAT) were utilized. As detailed in the Experimental section, these precursors exhibited high solubility in solvents such as toluene and oleylamine (OLA). To minimize temperature fluctuations during hot injection, OLA (a high-boiling solvent) was used to solubilize the metal precursors. The miscibility of the components in OLA is likely due to coordinate bonding. OLA's $-NH_2$ group can act as an electron donor, coordinating to the empty orbitals of Ba, Nb, or Ta, or perhaps an ammonolysis reaction occurs, resulting in the formation of M–NHR ligands with the release of $HNMe_2$. CS_2 was subsequently added to the metal precursor–OLA mixture, likely reacting with OLA to form an oleyldithiocarbamate species. The metal precursors remain dissolved in the solution after the addition of CS_2, and metal oleyldithiocarbamate species likely form in the solution along with the loss of $HNMe_2$. The dissolution of metal oleyldithiocarbamate species was likely aided by the long carbon chains, as direct CS_2 insertion into organobarium and amide species of Ta or Nb would likely form dithiocarboxylate and dithiocarbamate species, respectively. According to our previous reports, these species are not soluble in commonly used polar solvents—except for pyridine at room temperature—for Ba, Ti, Zr, and Hf species.[17,35] Notably, the solution's viscosity increased with increasing CS_2 concentration up to nearly an OLA : CS_2 ratio of 1 : 2, though we limited the CS_2-to-OLA molar ratio to 1 : 1 in our experiments. The hydrophobic interactions may also occur between the nonpolar hydrocarbon tails of OLA and the ligands in the metal–organic compounds.

For both Ba–Nb–S and Ba–Ta–S systems, identical methodologies, precursor quantities, and synthesis temperatures (up to 375 °C, the maximum achievable with mineral oil due to vigorous solvent reflux) were employed. Upon injection of the OLA–metal precursors–CS_2 into hot mineral oil, a rapid nucleation of nanocrystals occurred, yielding a dense brownish-black reaction medium. After a 30-minute dwell time, the products were washed with toluene and isopropanol, and further analyses were performed on drop-cast nanocrystal films.

The result of phase-pure $BaTaS_3$ nanocrystals is supported *via* X-ray diffraction (XRD) (Fig. 3a), while the Ba–Nb–S product appeared to contain minor NbS_2 impurities (Fig. 3d). This may arise from the niobium-deficient composition $BaNb_{0.98}S_3$, resulting in a mixture of dominant $BaNb_{0.98}S_3$ and trace NbS_2. Nevertheless, the rod-like morphology observed in transmission electron microscopy (TEM) images (Fig. 3b and e) for both $BaTaS_3$ and $BaNb_{0.98}S_3$ is promising for applications originating from material anisotropy. High-resolution transmission electron microscopy (HRTEM) analysis revealed preferential crystal growth along the [001] direction along its long axis (Fig. 3c, f, S1 and S2). This orientation, if further optimized by tuning reaction parameters to enhance nanocrystal length, could prove advantageous for applications where crystal anisotropy is favored. Scanning transmission electron microscopy-energy dispersive X-ray spectroscopy (STEM-EDX) analysis in Fig. 4a and b also confirmed the exclusive presence of Ba–Nb–S and Ba–Ta–S in the nanocrystals. Since these nanocrystals could find applications in optical technologies, we estimated their bandgaps using UV-vis measurements. The Kubelka–Munk transformation of the diffuse reflectance data estimated direct bandgap values of 1.73 eV for $BaNb_{0.98}S_3$ and 1.68 eV for $BaTaS_3$, respectively, which were lower than their indirect bandgap counterparts, signifying that these materials have a direct bandgap (Fig. 5a and b). These trends are in agreement with $BaTiS_3$ and $Sr_{1.143}TiS_3$, which are also reported as direct bandgap materials. Nonetheless, additional theoretical work is needed to determine the band structures of these materials and the energy levels constituting the valence band maximum and conduction band minimum.

In a separate reaction, a hot injection of metal precursors, OLA, and CS_2 was performed into hot OLA maintained at 340 °C to observe any differences in morphology. Fig. S3 shows that $BaTaS_3$ nanocrystals were obtained in this case as well. Interestingly, the morphology remained the same, with slightly smaller nanocrystals. This indicates that reaction conditions can be adjusted to modify the morphology of $BaTaS_3$ nanocrystals.

Synthesis of $BaMSe_3$ and $Ba_3N_2Se_9$ nanocrystals (M = Ti, Zr; N = Nb, Ta)

Next, we report the first instance in which nanocrystals of selenide members of the $ABSe_3$ family have been synthesized. We employed two different methods for this purpose: a heat-up reaction using elemental selenium and a hot injection reaction utilizing selenourea as the selenium precursors. Elemental selenium was preferred due to selenourea's higher cost and limited solubility in OLA at room temperature. Other selenium precursors, such as $SeCl_4$, were avoided to prevent the potential formation of secondary Ba–Cl phases which are known to be highly thermodynamically favorable.[36]

As detailed in the Experimental section, selenium does not dissolve in OLA at room temperature; therefore, a heat-up reaction with OLA was conducted. Heat-up reactions are generally less likely to yield oriented nanocrystals compared to hot injection methods as the monomer generation is more gradual which can sometimes make it harder to achieve highly anisotropic shapes unless the precursor chemistry, stabilizers, and heating rates are carefully chosen to control nucleation and growth.[37–39] However, these variables were not explicitly investigated in this study.

$BaTiS_3$ has been extensively studied among hexagonal chalcogenide perovskites, but its selenide counterpart, $BaTiSe_3$, which also crystallizes in hexagonal structure, remains largely unexplored. Moreover, no prior reports exist of its low-to-moderate-temperature synthesis. Here, we successfully synthesized $BaTiSe_3$ nanocrystals at 340 °C.

Metal precursors (Cp^*_2Ba and TEMAT), selenium, and OLA were heated together, nucleating black Ba–Ti–Se nanocrystals. Froth formation followed by the reaction solution turning opaque indicated nucleation at ~250 °C, but the temperature

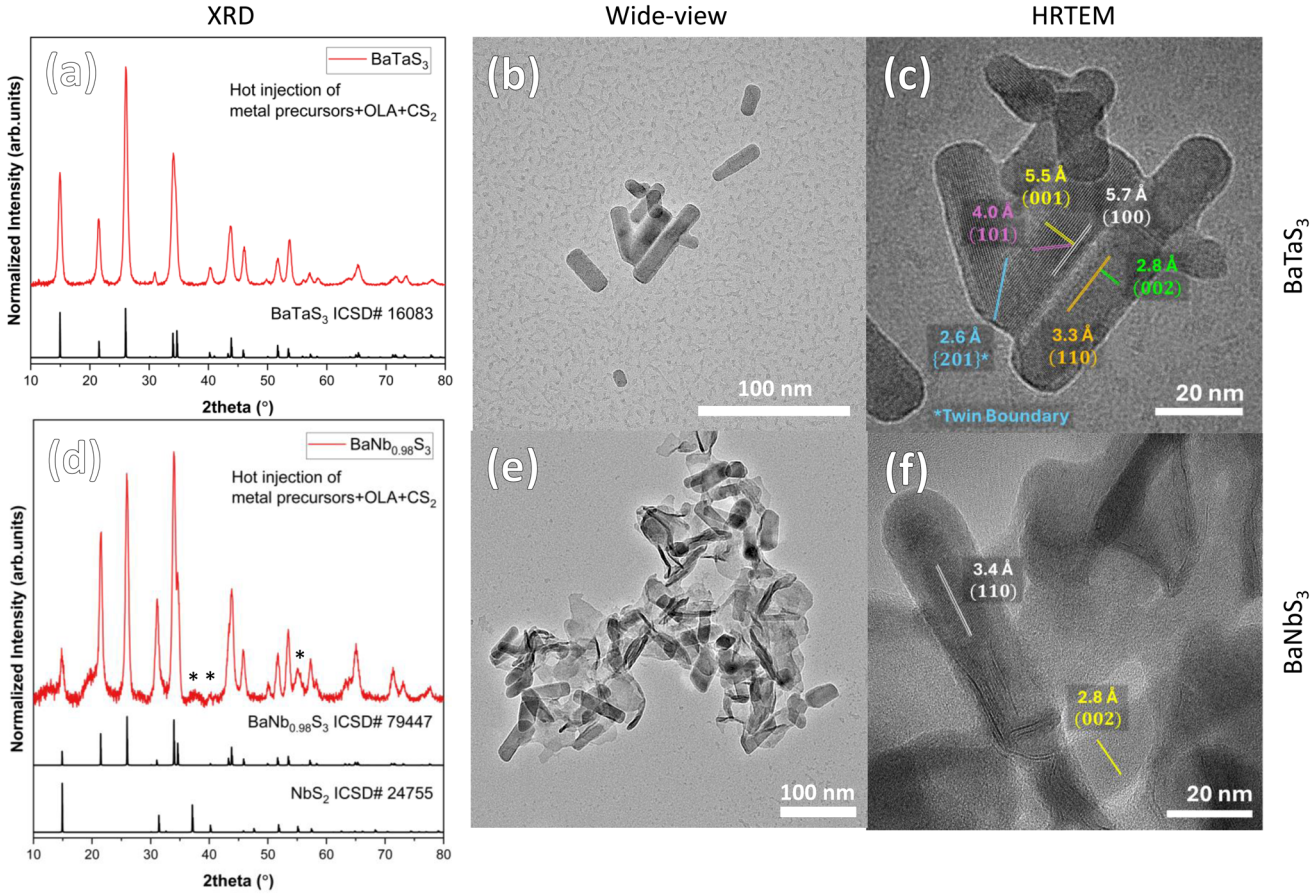

Fig. 3 Ba–M–S nanocrystals synthesized *via* the methods discussed are shown here. In (a and b) are $BaTaS_3$ nanocrystals, showing a rather distinct shape anisotropy in their rod-like structure. These nanorods prefer to grow along the [001] direction along its long axis. In (c), crystal twinning is also shown to be present along {201} boundary. In (d and e) are the nanocrystals from the procedure used to synthesize $BaNbS_3$. Two distinct structures can be seen in (e and f): the rod-like structures (determined to be the hexagonal $BaNbS_3$ nanorods) and ribbon- or sheet-like structures which are assumed to be NbS_2. Possible NbS_2 reflections are marked * in (d). NbS_2 is known to form as nanosheets when synthesized in OLA.[34]

was raised to 340 °C to promote nanocrystal growth. XRD results (Fig. 6a) supports the synthesis of phase-pure $BaTiSe_3$. However, TEM revealed spherical nanocrystals instead of the expected rod-like morphology (Fig. 6b and c). This was attributed to the rapid breakdown of the selenium precursor during heating, generating reactive monomers that drove kinetically controlled spherical growth. The Fast Fourier Transform (FFT) analysis of the HRTEM image, discussed in detail in Fig. S4a, further support the achievement of the correct phase of $BaTiSe_3$.

In the second method, a selenourea–OLA–metal precursor solution was hot-injected into mineral oil at 375 °C, resulting in the formation of $BaTiSe_3$ nanocrystals, as confirmed by XRD in Fig. S5. The selenourea–OLA dissolution process is detailed in the Experimental methods section. HRTEM (Fig. S6) shows that this method also produced irregular, predominantly spherical nanocrystals without preferred orientation. This contrasts with the findings of Zilevu *et al.*,[15] who observed $BaTiS_3$ nanorods using hot-injection synthesis and nanoparticles through heat-up reactions, indicating a potential difference in decomposition pathways between the different chalcogens. While achieving the first synthesis of $BaTiSe_3$ nanocrystals is significant, future studies should optimize reaction parameters, such as precursor reactivity and surfactant selection to achieve rod-like morphologies, which are of greater interest to the research community.

Similar heat-up and hot injection methods were applied to synthesize $SrTiSe_3$ nanocrystals (shown in Fig. S7 and S8), inspired by the promising properties of $SrTiS_3$. However, both methods resulted in binary phases below 400 °C, suggesting either ternary instability at lower temperatures or premature nucleation of metal–selenium monomers leading to binary selenides.[3]

For $BaZrSe_3$ synthesis, hot injection of metal precursors and OLA into OLA with selenium at 340 °C with 30-minute dwell time resulted in hexagonal $BaZrSe_3$ nanoparticles (as shown in Fig. S9), Tranchitella *et al.* have reported the synthesis of $Ba_{15}Zr_{14}Se_{12}$ by solid-state reaction.[40] However, the pXRD pattern of the synthesized nanocrystals aligns more closely with that of $BaZrSe_3$. Interestingly, the heat-up reaction of metal precursors, OLA, and selenium at 340 °C produced binary selenides. Surprisingly, hot injection reactions using selenourea as the selenium source, into both OLA and mineral oil at 340 °C and 375 °C, resulted in an unidentified phase that could not be matched with any known Ba, Zr, or Se binary or ternary

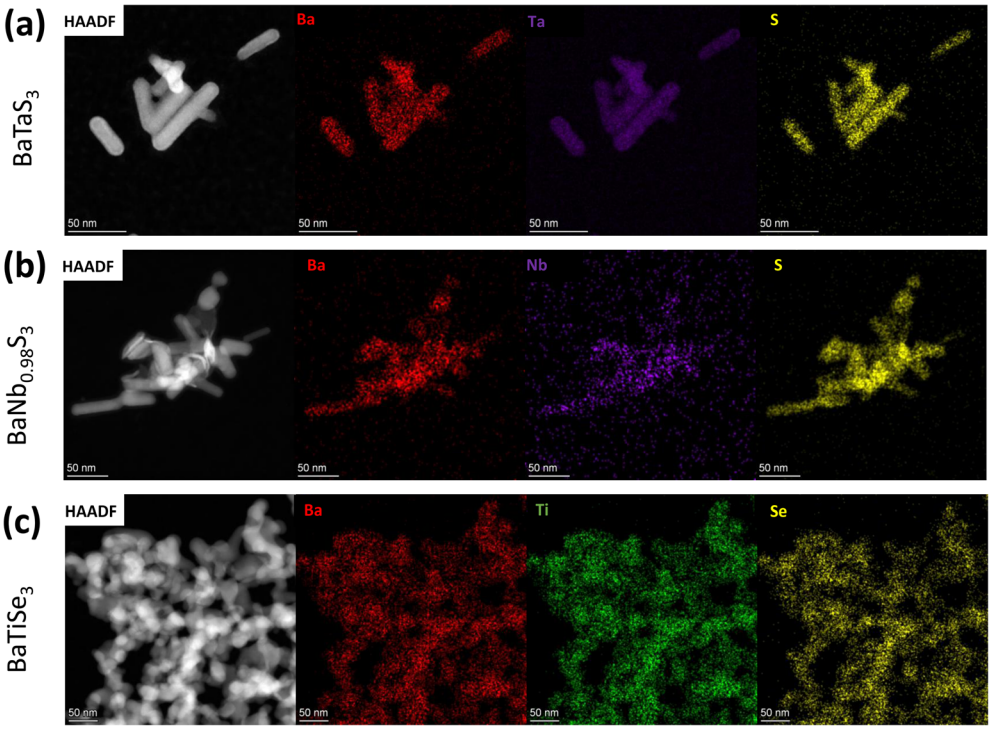

Fig. 4 STEM-EDX emission maps of the different nanocrystals showcase a uniform distribution of elements: (a) $BaTaS_3$, (b) $BaNb_{0.98}S_3$, and (c) $BaTiSe_3$. Since the Nb-L and S-K lines overlap, Nb-K lines were used for the EDX analysis.

compounds (see Fig. S10 and S11). While it is possible that a new metastable phase was synthesized, further work is required to confirm this.

Similar to $BaNbS_3$ and $BaTaS_3$, $BaNbSe_3$ and $BaTaSe_3$ are also reported to crystallize in hexagonal structures. However, like their sulfide counterparts, these selenides remain understudied and could be promising candidates for optoelectronic applications. We employed both previously discussed methods, the heat-up reaction with selenium and the hot injection method with selenourea but failed to obtain the desired 1 : 1:3 ternary phase. The heat-up reaction was performed at a maximum temperature of 340 °C using OLA as the reaction solvent, while the hot injection method was carried out at 375 °C by injecting a solution containing OLA, selenourea, and metal precursors into hot mineral oil, followed by a 30-minute dwell time. Instead, for both compounds and methods, a ternary phase with stoichiometry $Ba_3N_2Se_9$ (N = Nb, Ta) in a monoclinic structure formed, even when starting with a 1 : 1 molar ratio of metal precursors (see Fig. 6d, S12a, S13 and S14).[26] In one experiment with a 1 : 1 Ba : Ta molar ratio *via* hot injection, a mixture of $BaTaSe_3$, $Ba_3Ta_2Se_9$, and binary selenides formed (Fig. S15). However, the lack of reproducibility of this

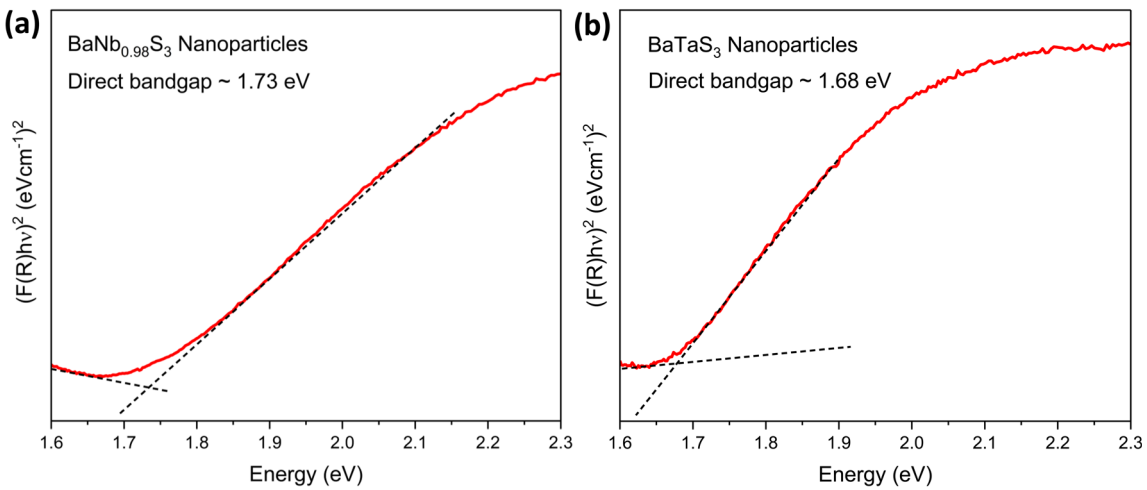

Fig. 5 Kubelka–Munk transformation of the diffuse reflectance data for (a) $BaNb_{0.98}S_3$ and (b) $BaTaS_3$ nanocrystals.

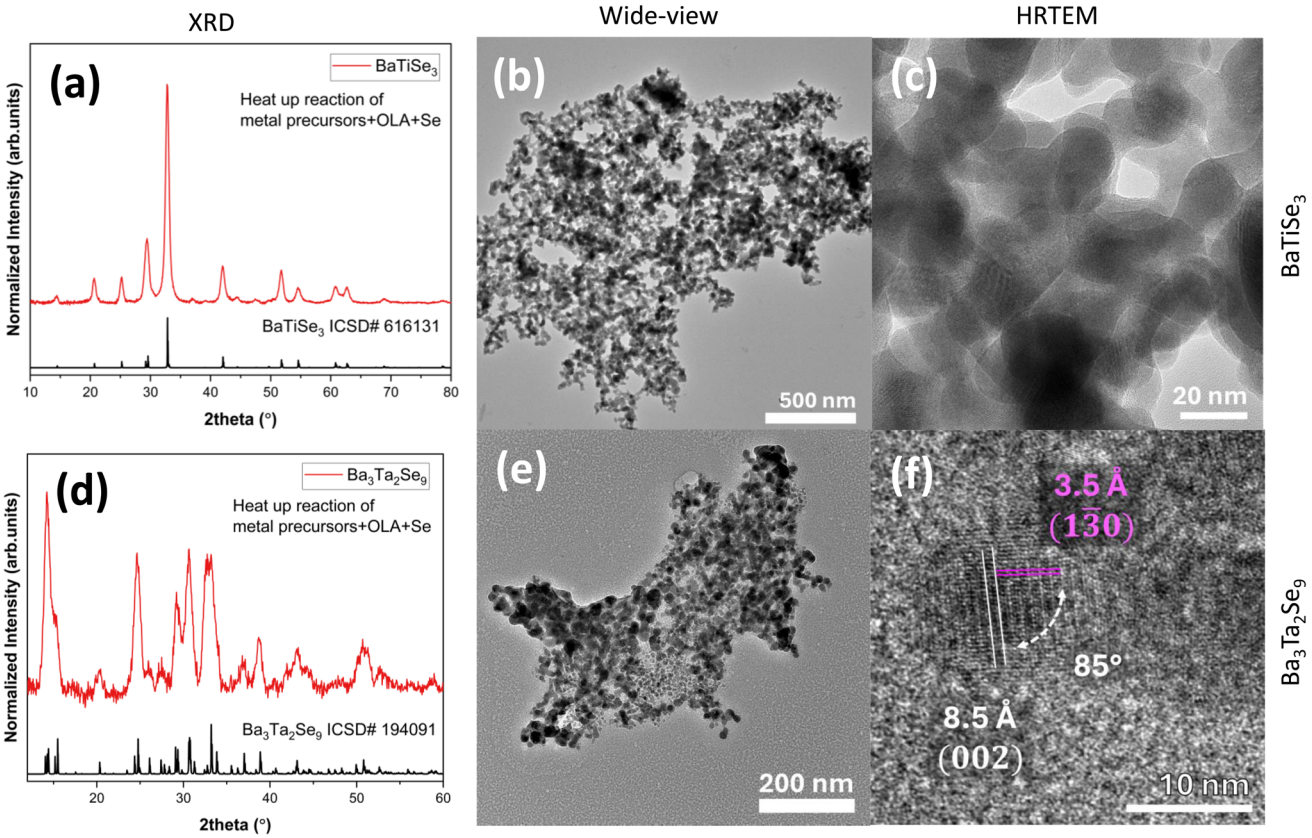

Fig. 6 Ba–M–Se nanocrystals synthesized *via* the methods discussed are shown here. $BaTiSe_3$ is shown in (a–c), $Ba_3Ta_2Se_9$ is shown in (d–f). The $BaTiSe_3$ presented here was synthesized *via* the reaction method where elemental Se was heated up with metal precursors. Due to the significant aggregation and overlap of $BaTiSe_3$ NCs in (c), we leave the visible lattice fringes unlabeled. An FFT analysis is provided in the SI for (c).

experiment and the mixed-phase outcomes suggest that $BaTaSe_3$ is likely not the thermodynamically favored phase under these reaction conditions.

To test the hypothesis that differential solubility of metal precursors might favor $Ba_3Ta_2Se_9$ formation, we varied the Ba : Ta stoichiometry from 0.8 : 1 to 1.5 : 1 while using hot injection method. However, all reactions resulted in $Ba_3Ta_2Se_9$ as the major product, with the remainder likely being amorphous species (shown in Fig. S16 and S17). This indicates that $BaNbSe_3$ and $BaTaSe_3$ are likely not thermodynamically stable under any of the reaction conditions used in this study.

Nonetheless, $Ba_3Nb_2Se_9$ and $Ba_3Ta_2Se_9$ exhibit favorable bandgaps of 1.3 eV and 1.6 eV, respectively, making them exciting candidates for optoelectronic applications such as photovoltaics and photodetectors.[26] TEM imaging shown in Fig. 6e, f, S18, S12b and c revealed that $Ba_3Ta_2Se_9$ and $Ba_3Nb_2Se_9$ nanocrystals synthesized with 3 : 2 metal ratios were polydisperse in size, complicating lattice plane assignment. While $Ba_3Ta_2Se_9$ lattice planes were successfully identified (Fig. 6f and S18), similar analysis for $Ba_3Nb_2Se_9$ proved inconclusive with the images collected.

Conclusions

In summary, this study highlights the successful chemistry involving organometallic precursors and CS_2 as the sulfur source to synthesize $BaNb_{0.98}S_3$ and $BaTaS_3$ hexagonal ABX_3, which could find utility in optical applications because of their rod-like morphology. Moreover, for the first time, we have reported the successful demonstration of routes for the synthesis of selenide members of the chalcogenide perovskite family. Phase-pure $BaTiSe_3$ has been synthesized using both elemental selenium and selenourea as selenium precursors, and $BaZrSe_3$ nanocrystals have also been obtained *via* a hot injection route. Similarly, $Ba_3TM_2Se_9$ (TM = Nb, Ta) nanocrystals have been synthesized, all of which possess suitable bandgaps for optoelectronic applications such as photovoltaics.

Experimental methods

Materials

Carbon disulfide (CS_2, anhydrous, >99%), pyridine (Pyd, anhydrous, 99.8%), *N*,*N*-dimethylformamide (DMF, anhydrous, 99.8%), molecular sieves (type 3A, bead size 8–12 mesh), tetrakisethylmethylamido titanium(IV) (TEMAT, >99.999%), oleylamine (OLA) (technical grade, 70%; OLA), toluene (anhydrous, 99.8%), isopropanol (anhydrous, 99.5%; IPA), calcium hydride (95%; CaH_2), 2-methyl-2-propanethiol (99%), selenourea (98%), selenium powder (99.99%) were purchased from Sigma Aldrich. Pentakis(dimethylamino)niobium(V) (PDMAN, 99%) and pentakis(dimethylamino)tantalum(V) (PDMAT, >98%) were

purchased from STREM Chemicals. High purity mineral oil was purchased from Fisher Scientific.

Purification of materials prior to use

Before experimental use, many of the materials underwent various purification steps.[17] Molecular sieves were dried overnight under vacuum at 100 °C prior to use. Mineral oil was subjected to freeze–pump–thaw cycles before being stored over dried molecular sieves. OLA was purified by freeze–pump–thaw cycles, dried with CaH_2, distilled to remove residual CaH_2, and then stored over dried molecular sieves inside a nitrogen-filled glovebox. All glassware used for purification, drying, or storage was dried in a vacuum oven under partial vacuum (~800 mbar) in an argon atmosphere at 150 °C for at least 30 minutes before use.

All chemicals were stored in nitrogen-filled gloveboxes and handled exclusively within the gloveboxes.

Characterization

X-ray diffraction (XRD) analysis was conducted using a Rigaku SmartLab diffractometer under ambient conditions, employing parallel beam geometry with an incident beam angle of 0.5°. Data collection utilized a Cu Kα source ($\lambda = 1.5406$ Å) operated at 40 kV and 44 mA.

Transmission electron microscopy (TEM) samples were prepared by drop-casting a diluted solution of nanoparticles in toluene onto a copper grid and allowing them to dry naturally in air. TEM, STEM-HAADF imaging, and STEM-EDX analyses were performed using an FEI Talos F200i scanning/transmission electron microscope (S/TEM) operated at an accelerating voltage of 200 kV.

Metal sulfide nanocrystals synthesis

The synthesis method was adapted from our previous study, where we first reported the reproducible synthesis of phase-pure $BaZrS_3$.[17] However, we modified the protocol slightly to facilitate the precise injection of metal precursors in the desired ratios.

We began by adding 3 mL of commercially available mineral oil to a 3-neck round-bottom flask. An Allihn condenser was attached to one port, a thermocouple adapter and heating jacket to another, and a rubber septum secured with steel lockwire to the third.

Separately, a solution of metal precursors in OLA was prepared. Metal precursors were weighed into a vial (the amount of barium was kept constant at 0.16 mmol, while the amount of the other metal precursor was varied according to the targeted stoichiometry), followed by the addition of 2 mL OLA. The mixture was stirred until complete dissolution occurred (1–2 hours). Next, 600 μL of CS_2 was added dropwise, resulting in a reaction between OLA and CS_2 to form a viscous dithiocarbamic species. Despite this, the mixture remained a single-phase solution.

This solution was transferred to a single-neck round-bottom flask, sealed with a rubber septum and steel lockwire, and set aside. The 3-neck flask containing mineral oil was connected to a Schlenk line, and three vacuum–argon purge cycles were performed to remove oxygen from the headspace. The flask was then heated to the target temperature (375 °C) using a heating mantle. Meanwhile, the OLA–metal precursor–CS_2 mixture was warmed to 60 °C to reduce its viscosity.

Once the mineral oil reached the target temperature and stabilized, the precursor solution was drawn into a syringe and hot-injected into the mineral oil, triggering rapid nanocrystal nucleation. The reaction was held at temperature for 30 minutes before cooling naturally to room temperature.

Metal selenide nanocrystals synthesis

Two different methods were used for synthesizing selenide-based nanoparticles, differing primarily in the selenium precursor used: selenourea or elemental selenium powder.

Method 1: selenourea as precursor. 1 mmol of selenourea was dissolved in 3 mL of OLA using a solvothermal microwave reactor at 200 °C. The selenourea likely decomposed during heating, as residual pressure was observed in the microwave vial. However, the resulting solution contained a dissolved selenium phase different from elemental selenium dissolved directly in OLA. Metal precursors (the amount of barium was kept constant at 0.16 mmol, while the amount of the other metal precursor was varied according to the targeted stoichiometry) were added to the selenourea–OLA solution in a nitrogen-filled glovebox and stirred overnight, yielding a homogeneous mixture. The presence of metal–selenium bonds at this stage is unclear.

3 mL of mineral oil was added to a 3-neck flask configured as described in the CS_2 case (Allihn condenser, thermocouple adapter, rubber septum).

The setup was purged *via* three vacuum–argon cycles on a Schlenk line, heated to the target temperature (*e.g.*, 375 °C), and stabilized. The precursor solution was then hot-injected into the mineral oil, initiating rapid nucleation of metal selenide nanocrystals.

Method 2: elemental selenium powder as precursor. Metal precursors (the amount of barium was kept constant at 0.16 mmol, while the amount of the other metal precursor was varied according to the targeted stoichiometry), 4 mL of OLA, and 1 mmol of selenium powder were combined directly in a 3-neck flask. A glass stopper (instead of a rubber septum) was used to seal the third port. The setup was assembled in a glovebox, transferred to a Schlenk line, and purged with argon. The mixture was heated to the target temperature (340 °C), allowing nanocrystal nucleation. The temperature was maintained for 30 minutes before cooling.

Please note that selenium powder has limited solubility in OLA at room temperature and hence, a hot injection reaction was not performed; dissolution at 200–250 °C was not attempted here.

Synthesis of $BaZrSe_3$ nanocrystals

The method used to synthesize $BaZrSe_3$ nanocrystals differs from the approaches discussed above. While the previous methods were unsuccessful, a hot injection reaction of metal precursors and OLA into OLA with selenium was performed. The metal precursors (with the amount of barium kept constant

at 0.16 mmol and the amount of the other metal precursor varied according to the targeted stoichiometry) were mixed with 2 mL of OLA in a nitrogen-filled glovebox and stirred overnight to yield a homogeneous mixture. Separately, 3 mL of OLA and 1 mmol of selenium powder were added to a three-neck flask configured as described for the CS_2 case (with an Allihn condenser, thermocouple adapter, and rubber septum).

The setup was purged with three vacuum–argon cycles on a Schlenk line, heated to the target temperature (*e.g.*, 340 °C), and allowed to stabilize. The precursor solution was then hot-injected into the OLA, initiating rapid nucleation of metal selenide nanocrystals.

Nanocrystals washing and storage

Following the reaction in all the above cases, the setup was transferred to a nitrogen-filled glovebox, and the nanocrystals were washed using the procedure outlined in our prior work. The nanoparticle solution was then transferred from the reaction flask to a centrifuge tube, followed by the addition of 3 mL of toluene and vortexing to obtain a homogeneous solution. Approximately 18 mL of isopropanol was then added, and the mixture was vortexed again. The centrifuge tube was capped, and the mixture was centrifuged at 14 000 rpm for 5 minutes, resulting in the separation of nanocrystals from the solution. The supernatant was decanted, and the collected nanoparticles were redispersed in 3 mL of toluene, followed by the addition of 18 mL of isopropanol and centrifugation once more. This process was repeated a total of three times. Finally, the nanocrystals collected in the centrifuge tube were redispersed in 1 mL of toluene and stored.

Author contributions

S. Agarwal: writing – original draft, writing – review & editing, validation, methodology, formal analysis, data curation, visualization, conceptualization. S. Rodriguez: writing – review & editing, validation, methodology, investigation, formal analysis, data curation. M. R. Marques: writing – review & editing, validation, methodology, investigation, formal analysis, data curation. D. C. Hayes: writing – review & editing, formal analysis, data curation. K. C. Vincent: writing – review & editing, formal analysis, data curation. R. Agrawal: writing – review & editing, validation, supervision, resources, methodology, funding acquisition.

Conflicts of interest

The authors declare no conflict of interest.

Data availability

The data supporting this article have been included in the SI. Supplementary information: Additional X-ray diffraction, TEM, HRTEM and HAADF-STEM data. See DOI: https://doi.org/10.1039/d5na00628g.

Acknowledgements

The authors acknowledge the National Science Foundation's financial support through grant 2422591 (DMR).

References

1 M. Chhowalla, D. Jena and H. Zhang, Two-Dimensional Semiconductors for Transistors, *Nat. Rev. Mater.*, 2016, **1**(11), 16052, DOI: 10.1038/natrevmats.2016.52.
2 X. Huang, C. Liu and P. Zhou, 2D Semiconductors for Specific Electronic Applications: From Device to System, *npj 2D Mater. Appl.*, 2022, **6**(1), 51, DOI: 10.1038/s41699-022-00327-3.
3 K. V. Sopiha, C. Comparotto, J. A. Márquez and J. J. S. Scragg, Chalcogenide Perovskites: Tantalizing Prospects, Challenging Materials, *Adv. Opt. Mater.*, 2022, **10**(3), 2101704, DOI: 10.1002/adom.202101704.
4 S. Agarwal, K. C. Vincent and R. Agrawal, From Synthesis to Application: A Review of $BaZrS_3$ Chalcogenide Perovskites, *Nanoscale*, 2025, **17**(8), 4250–4300, DOI: 10.1039/D4NR03880K.
5 S. Niu, G. Joe, H. Zhao, Y. Zhou, T. Orvis, H. Huyan, J. Salman, K. Mahalingam, B. Urwin, J. Wu, Y. Liu, T. E. Tiwald, S. B. Cronin, B. M. Howe, M. Mecklenburg, R. Haiges, D. J. Singh, H. Wang, M. A. Kats and J. Ravichandran, Giant Optical Anisotropy in a Quasi-One-Dimensional Crystal, *Nat. Photonics*, 2018, **12**(7), 392–396, DOI: 10.1038/s41566-018-0189-1.
6 J. Wu, X. Cong, S. Niu, F. Liu, H. Zhao, Z. Du, J. Ravichandran, P. Tan and H. Wang, Linear Dichroism Conversion in Quasi-1D Perovskite Chalcogenide, *Adv. Mater.*, 2019, **31**(33), 1902118, DOI: 10.1002/adma.201902118.
7 F. Yang, K. Li, M. Fan, W. Yao, L. Fu, C. Xiong, S. Jiang, D. Li, M. Xu, C. Chen, G. Zhang and J. Tang, Strongly Anisotropic Quasi-1D $BaTiS_3$ Chalcogenide Perovskite for Near-Infrared Polarized Photodetection, *Adv. Opt. Mater.*, 2023, **11**(5), 2201859, DOI: 10.1002/adom.202201859.
8 B. Zhao, M. S. B. Hoque, G. Y. Jung, H. Mei, S. Singh, G. Ren, M. Milich, Q. Zhao, N. Wang, H. Chen, S. Niu, S.-J. Lee, C.-T. Kuo, J.-S. Lee, J. A. Tomko, H. Wang, M. A. Kats, R. Mishra, P. E. Hopkins and J. Ravichandran, Orientation-Controlled Anisotropy in Single Crystals of Quasi-1D $BaTiS_3$, *Chem. Mater.*, 2022, **34**(12), 5680–5689, DOI: 10.1021/acs.chemmater.2c01046.
9 S. F. Gillani, N. Yasmin, Z. Usman, H. M. Khan, M. Safdar and M. Mirza, First Principles Study on Optical and Thermal Properties of $BaTiS_3$, *Optik*, 2022, **261**, 169196, DOI: 10.1016/j.ijleo.2022.169196.
10 T. R. Paudel and E. Y. Tsymbal, Evaluating the Thermoelectric Properties of $BaTiS_3$ by Density Functional Theory, *ACS Omega*, 2020, **5**(21), 12385–12390, DOI: 10.1021/acsomega.0c01139.
11 Y. Wang, L. Xie, H. Yang, M. Hu, X. Qian, R. Yang and J. He, Strong Orbital-Lattice Coupling Induces Glassy Thermal Conductivity in High-Symmetry Single Crystal $BaTiS_3$, *Phys.*

Rev. X, 2025, **15**(1), 011066, DOI: 10.1103/PhysRevX.15.011066.

12 H. Chen, B. Zhao, J. Mutch, G. Y. Jung, G. Ren, S. Shabani, E. Seewald, S. Niu, J. Wu, N. Wang, M. Surendran, S. Singh, J. Luo, S. Ohtomo, G. Goh, B. C. Chakoumakos, S. J. Teat, B. Melot, H. Wang, A. N. Pasupathy, R. Mishra, J. Chu and J. Ravichandran, Charge Density Wave Order and Electronic Phase Transitions in a Dilute d-Band Semiconductor, *Adv. Mater.*, 2023, **35**(49), 2303283, DOI: 10.1002/adma.202303283.

13 J. Liu, S. Zhang, M. Jiang, H. Xiao, S. Feng and L. Qiao, Electronic Structure and Anion Engineering for Perovskite Oxysulfide $BaTi(O,S)_3$, *J. Vac. Sci. Technol., A*, 2022, **40**(1), 012801, DOI: 10.1116/6.0001471.

14 K. Momma and F. Izumi, VESTA 3 for Three-Dimensional Visualization of Crystal, Volumetric and Morphology Data, *J. Appl. Crystallogr.*, 2011, **44**(6), 1272–1276, DOI: 10.1107/S0021889811038970.

15 D. Zilevu and S. E. Creutz, Shape-Controlled Synthesis of Colloidal Nanorods and Nanoparticles of Barium Titanium Sulfide, *Chem. Mater.*, 2021, **33**(13), 5137–5146, DOI: 10.1021/acs.chemmater.1c01193.

16 H. Chen, S. Singh, H. Mei, G. Ren, B. Zhao, M. Surendran, Y.-T. Wang, R. Mishra, M. A. Kats and J. Ravichandran, Molten Flux Growth of Single Crystals of Quasi-1D Hexagonal Chalcogenide $BaTiS_3$, *J. Mater. Res.*, 2024, **39**(13), 1901–1910, DOI: 10.1557/s43578-024-01379-5.

17 D. C. Hayes, S. Agarwal, K. C. Vincent, I. M. Aimiuwu, A. A. Pradhan, M. C. Uible, S. C. Bart and R. Agrawal, A Reliable, Colloidal Synthesis Method of the Orthorhombic Chalcogenide Perovskite, $BaZrS_3$, and Related ABS_3 Nanomaterials (A = Sr, Ba; B = Ti, Zr, Hf): A Step Forward for Earth-Abundant, Functional Materials, *Chem. Sci.*, 2025, **16**(3), 1308–1320, DOI: 10.1039/D4SC06116K.

18 H. Mei, G. Ren, B. Zhao, J. Salman, G. Y. Jung, H. Chen, S. Singh, A. S. Thind, J. Cavin, J. A. Hachtel, M. Chi, S. Niu, G. Joe, C. Wan, N. Settineri, S. J. Teat, B. C. Chakoumakos, J. Ravichandran, R. Mishra and M. A. Kats, Colossal Optical Anisotropy from Atomic-Scale Modulations, *Adv. Mater.*, 2023, **35**(42), 2303588, DOI: 10.1002/adma.202303588.

19 Y. Han, J. Zhang, Z. Yu, J. Zhu, X. Xing, Q. Mo, L. Li, H. Gao, X. Chen, Z. Ma, J. Zhang, Y. Zhang, M. Li and Z. Shi, Integration of Photo- and Thermal-Detection Based on Hexagonal Chalcogenide Perovskite $Sr_8Ti_7S_{21}$ with Full Spectrum Absorption, *Adv. Funct. Mater.*, 2025, **35**, 2500792, DOI: 10.1002/adfm.202500792.

20 B. Zhao, H. Mei, Z. Du, S. Singh, T. Chang, J. Li, B. Ilyas, Q. Song, T. Liu, Y. Shao, R. Comin, N. Gedik, N. S. Settineri, S. J. Teat, Y. Chen, S. B. Cronin, M. A. Kats and J. Ravichandran, Infrared Optical Anisotropy in Quasi-1D Hexagonal Chalcogenide $BaTiSe_3$, *Adv. Opt. Mater.*, 2024, **12**(29), 2400327, DOI: 10.1002/adom.202400327.

21 M. Saeki and M. Onoda, Preparation of a Chain-Type Composite Crystal, Ba_xTiS_3 (x = 1.00–1.05), *J. Solid State Chem.*, 1994, **112**(1), 65–69, DOI: 10.1006/jssc.1994.1265.

22 M. Saeki, M. Onoda and Y. Yajima, Composite Crystals $BaTiS_y$ (y = 2.70–2.93), *J. Solid State Chem.*, 1996, **121**(2), 451–456, DOI: 10.1006/jssc.1996.0062.

23 S.-J. Kim, H.-S. Bae, K.-A. Yee, J.-H. Choy, D.-K. Kim and N.-H. Hur, Structure and Physical Properties of the Barium Niobium Sulfides $BaNbS_3$ and $BaNb_{0.8}S_{3-\delta}$, *J. Solid State Chem.*, 1995, **115**(2), 427–434, DOI: 10.1006/jssc.1995.1155.

24 O. Gourdon, L. Cario, V. Petricek, J. M. Perez-Mato and M. Evain, Synthesis, Structure Determination, and Twinning of Two New Composite Compounds in the Hexagonal Perovskite-like Sulfide Family: $Eu_{8/7}TiS_3$ and $Sr_{8/7}TiS_3$, *Z. Kristallogr. – Cryst. Mater.*, 2001, **216**(10), 541–555, DOI: 10.1524/zkri.216.10.541.20366.

25 N. E. Ingram, B. J. Jordan, B. Donnadieu and S. E. Creutz, Barium and Titanium Dithiocarbamates as Precursors for Colloidal Nanocrystals of Emerging Optoelectronic Materials, *Dalton Trans.*, 2021, **50**(44), 15978–15982, DOI: 10.1039/D1DT03018C.

26 M.-Y. Chung and C.-S. Lee, $Ba_3TM_2Se_9$ (TM = Nb, Ta): Synthesis and Characterization of New Polyselenides, *Inorg. Chem.*, 2014, **53**(1), 80–84, DOI: 10.1021/ic4013763.

27 R. A. Gardner, M. Vlasse and A. Wold, Electrical Properties and Crystal Structure of Barium Tantalum Sulfide, $BaTaS_3$, *Inorg. Chem.*, 1969, **8**(12), 2784–2787, DOI: 10.1021/ic50082a049.

28 J. J. Neumeier and M. G. Smith, Superconductivity in Quasi-One-Dimensional $BaNbS_3$, *Phys. C*, 2017, **542**, 1–5, DOI: 10.1016/j.physc.2017.08.006.

29 M. Ishii and M. Saeki, Raman and Infrared Spectra of $BaTiS_3$ and $BaNbS_3$, *Phys. Status Solidi B*, 1992, **170**(1), K49–K54, DOI: 10.1002/pssb.2221700149.

30 A. Yu. Grippa, O. G. D'yachenko, A. M. Abakumov and E. V. Antipov, Crystal Structure of $BaNb_{0.9}S_3$, *Crystallogr. Rep.*, 2001, **46**(3), 373–376, DOI: 10.1134/1.1376462.

31 T. Ohtani, H. Sawada and M. Chikamori, Phase Transitions in Quasi-One-Dimensional Chalcogenides of $BaNb_xS_3$ and $BaTa_xSe_3$, *Mater. Res. Bull.*, 2004, **39**(4–5), 561–569, DOI: 10.1016/j.materresbull.2003.12.015.

32 B.-H. Chen, G. Sàghi-Szabó, B. Eichhorn, J.-L. Peng and R. Greene, Synthesis, Structure and Properties of Barium Niobium Triselenide, *Mater. Res. Bull.*, 1992, **27**(10), 1249–1253, DOI: 10.1016/0025-5408(92)90233-P.

33 T. Ohtani, S. Honji and M. Takano, Phase Transitions in Quasi-One-Dimensional Selenide $BaNbSe_3$ and Superconductivity in $BaNb_2Se_5$, *J. Solid State Chem.*, 1997, **132**(1), 188–195, DOI: 10.1006/jssc.1997.7443.

34 A. Mansouri and N. Semagina, Colloidal Synthesis Protocol of Shape- and Dimensionally-Controlled Transition-Metal Chalcogenides and Their Hydrodesulfurization Activities, *ACS Appl. Nano Mater.*, 2018, **1**(9), 4408–4412, DOI: 10.1021/acsanm.8b01353.

35 A. A. Pradhan, M. C. Uible, S. Agarwal, J. W. Turnley, S. Khandelwal, J. M. Peterson, D. D. Blach, R. N. Swope, L. Huang, S. C. Bart and R. Agrawal, Synthesis of $BaZrS_3$ and $BaHfS_3$ Chalcogenide Perovskite Films Using Single-Phase Molecular Precursors at Moderate Temperatures,

Angew. Chem., Int. Ed., 2023, **62**(15), e202301049, DOI: **10.1002/anie.202301049**.

36 S. Agarwal, K. C. Vincent and R. Agrawal, Quantitative Scales for Haliphilicity of Metals: Tailoring the Halide Affinity of Alkaline Earth Metals to Synthesize Chalcogenide Perovskite $BaMS_3$ (M = Zr, and Hf) and Cu_2BaSnS_4 Compounds, *ACS Appl. Energy Mater.*, 2024, **7**(22), 10584–10595, DOI: **10.1021/acsaem.4c02205**.

37 J. van Embden, A. S. R. Chesman and J. J. Jasieniak, The Heat-Up Synthesis of Colloidal Nanocrystals, *Chem. Mater.*, 2015, **27**(7), 2246–2285, DOI: **10.1021/cm5028964**.

38 S. G. Kwon and T. Hyeon, Formation Mechanisms of Uniform Nanocrystals via Hot-Injection and Heat-Up Methods, *Small*, 2011, **7**(19), 2685–2702, DOI: **10.1002/smll.201002022**.

39 M. Kulpa-Greszta, A. Tomaszewska, A. Dziedzic and R. Pązik, Rapid Hot-Injection as a Tool for Control of Magnetic Nanoparticle Size and Morphology, *RSC Adv.*, 2021, **11**(34), 20708–20719, DOI: **10.1039/D1RA02977K**.

40 L. J. Tranchitella, J. C. Fettinger, P. K. Dorhout, P. M. Van Calcar and B. W. Eichhorn, Commensurate Columnar Composite Compounds: Synthesis and Structure of $Ba_{15}Zr_{14}Se_{42}$ and $Sr_{21}Ti_{19}Se_{57}$, *J. Am. Chem. Soc.*, 1998, **120**(30), 7639–7640, DOI: **10.1021/ja972442p**.